AGU PUBLICATIONS

JGR

Journal of Geophysical Research: Solid Earth

RESEARCH ARTICLE
10.1002/2017JB014134

Key Points:
- We establish the optical signature of octahedrally coordinated low spin Fe^{3+} in iron-bearing new aluminous phase (NAL)
- The optical signature of low spin Fe^{3+} can be used to detect spin crossovers in bridgmanite and post-perovskite
- Crystal field considerations allow a spin transition in bridgmanite at P ~40 GPa

Supporting Information:
- Supporting Information S1

Correspondence to:
S. S. Lobanov and H. Hsu,
slobanov@carnegiescience.edu;
slobanov@igm.nsc.ru;
hanhsu@ncu.edu.tw

Citation:
Lobanov, S. S., H. Hsu, J.-F. Lin, T. Yoshino, and A. F. Goncharov (2017), Optical signatures of low spin Fe^{3+} in NAL at high pressure, *J. Geophys. Res. Solid Earth*, *122*, doi:10.1002/2017JB014134.

Received 27 FEB 2017
Accepted 28 APR 2017
Accepted article online 2 MAY 2017

Optical signatures of low spin Fe^{3+} in NAL at high pressure

Sergey S. Lobanov[1,2], Han Hsu[3], Jung-Fu Lin[4,5], Takashi Yoshino[6], and Alexander F. Goncharov[1,7]

[1]Geophysical Laboratory, Carnegie Institution of Washington, Washington, District of Columbia, USA, [2]Sobolev Institute of Geology and Mineralogy, Siberian Branch, Russian Academy of Sciences, Novosibirsk, Russia, [3]Department of Physics, National Central University, Taoyuan City, Taiwan, [4]Department of Geological Sciences, Jackson School of Geosciences, The University of Texas at Austin, Austin, Texas, USA, [5]Center for High Pressure Science and Technology Advanced Research (HPSTAR), Shanghai, China, [6]Institute for Planetary Materials, Okayama University, Misasa, Tottori, Japan, [7]Key Laboratory of Materials Physics, Institute of Solid State Physics, CAS, Hefei, China

Abstract The iron spin transition directly affects properties of lower mantle minerals and can thus alter geophysical and geochemical characteristics of the deep Earth. While the spin transition in ferropericlase has been documented at P ~60 GPa and 300 K, experimental evidence for spin transitions in other rock-forming minerals, such as bridgmanite and post-perovskite, remains controversial. Multiple valence, spin, and coordination states of iron in bridgmanite and post-perovskite are difficult to resolve with conventional spin probing techniques. Optical spectroscopy, on the other hand, can discriminate between high and low spin and between ferrous and ferric iron at different sites. Here we establish the optical signature of low spin $Fe^{3+}O_6$, a plausible low spin unit in bridgmanite and post-perovskite, by optical absorption experiments in diamond anvil cells. We show that the optical absorption of $Fe^{3+}O_6$ in new aluminous phase (NAL) is very sensitive to the iron spin state and may represent a model behavior of bridgmanite and post-perovskite across the spin transition. Specifically, an absorption band centered at ~19,000 cm^{-1} is characteristic of the $^2T_{2g} \rightarrow {}^2T_{1g}$ ($^2A_{2g}$) transition in low spin Fe^{3+} in NAL at 40 GPa, constraining the crystal field splitting energy of low spin Fe^{3+} to ~22,200 cm^{-1}, which we independently confirm by first-principles calculations. Together with available information on the electronic structure of $Fe^{3+}O_6$ compounds, we show that the spin-pairing energy of Fe^{3+} in an octahedral field is ~20,000–23,000 cm^{-1}. This implies that octahedrally coordinated Fe^{3+} in bridgmanite is low spin at $P >$ ~40 GPa.

1. Main Text

It has been reported that the spin transition of iron in lower mantle minerals can greatly impact physical and chemical properties of the deep Earth [*Badro*, 2014; *Badro et al*., 2003; *Lin et al*., 2013]. For example, high-pressure experiments at room temperature have identified anomalies in elastic and transport properties of ferropericlase (Fp) across the spin transition at P ~60 GPa [*Goncharov et al*., 2006; *Keppler et al*., 2007; *Marquardt et al*., 2009; *Yang et al*., 2015]) which may help elucidate seismic signatures and geodynamic processes of the lower mantle [*Huang et al*., 2015; *Marquardt et al*., 2009; *Vilella et al*., 2015; *Yang et al*., 2015]. It has also been proposed that the spin transition can affect the iron partitioning coefficient between mantle phases due to the associated decrease in iron's atomic volume [*Badro et al*., 2003; *Burns*, 1993]. Yet there are many unknowns in the exact role of spin transitions in the deep Earth.

Pressure-induced spin transitions have now been identified in multiple minerals that may be present in the lower mantle [*Badro*, 2014; *Lin et al*., 2013]. However, the mechanism, pressure, and compositional dependence of the spin state of bridgmanite (Bdgm), the most abundant lower mantle phase, remains controversial [*Badro et al*., 2004; *Catalli et al*., 2010, 2011; *Dorfman et al*., 2015; *Kupenko et al*., 2015; *Li et al*., 2004; *Lin et al*., 2012; *McCammon et al*., 2010; *Mohn and Trønnes*, 2016; *Zhang and Oganov*, 2006]. The main reason for this controversy arises from its crystal chemical complexity, in which the iron can be distributed between two nonequivalent crystallographic positions: large pseudododecahedral (*A*) sites and relatively small octahedral (*B*) sites [*McCammon*, 1997]. Ferric iron (Fe^{3+}) enters both *A* and *B* sites via charge-coupled substitution mechanism ($Fe^{3+} + Al^{3+} \rightarrow Si^{4+} + Mg^{2+}$ or $2Fe^{3+} \rightarrow Si^{4+} + Mg^{2+}$), while ferrous iron ($Fe^{2+}$) predominantly substitutes for Mg^{2+} at the *A* site [*Hummer and Fei*, 2012]. Importantly, aluminum admixture to the *B* site reduces its capacity to host ferric iron [*Kupenko et al*., 2015; *Potapkin et al*., 2013].

Theoretical investigations indicate that the *B*-site Fe^{3+} undergoes a transition from the high spin (HS) to the low spin (LS) state, while *A* site iron remains in the HS state, regardless of its valence [*Hsu and Wentzcovitch*, 2014; *Hsu et al*., 2012, 2010, 2011b; *Mohn and Trønnes*, 2016; *Yu et al*., 2012]. This theory-based view has found experimental support [*Catalli et al*., 2010, 2011; *Lin et al*., 2012] but is not yet widely accepted [*Kupenko et al.,* 2015; *McCammon et al*., 2010]. Earlier studies of the Bdgm spin state via X-ray emission spectroscopy (XES) [*Badro et al*., 2004; *Li et al*., 2004], a technique that is not site and valence specific, yielded an averaged spin moment for all iron ions at all possible crystallographic sites. Mőssbauer spectroscopy (traditional or synchrotron) can be used to infer the iron oxidation/spin states as well as the site occupancies, but the relation of hyperfine parameters to various iron states is not straightforward, and as a result, the interpretation of Mőssbauer spectra is generally inconclusive [*Dyar et al*., 2006]. Combined XES and Mössbauer studies helped to partially resolve the problem [*Catalli et al*., 2010, 2011; *Dorfman et al*., 2015; *Lin et al*., 2016] but are still inefficient in probing a broad range of chemical compositions because they require extraordinary access to synchrotron X-ray sources.

Alternatively, the spin and valence states of iron in a host mineral may be probed by optical absorption methods [*Burns*, 1993; *Keppler et al*., 2007; *Lobanov et al*., 2015, 2016a] which are fast (seconds to minutes, compared to hours for XES and Mősbauer) and do not require synchrotron sources. Unfortunately, at the time of previous optical studies of Bdgm [*Goncharov et al*., 2008; *Keppler et al*., 2008], the complexity of iron states in the mineral was not fully understood, and as a result, these studies did not explain how the optical spectra of Bdgm would change across various spin transition scenarios. Consequently, optical studies of the Bdgm spin state were discontinued.

The goal of this work is to address optical absorption and crystal field characteristics of mixed-valence iron-bearing minerals, such as Bdgm, across the spin transition. To this end, we use iron-bearing new aluminous phase (NAL) as a representative model of such compounds with a spin transition in $Fe^{3+}O_6$ at ~40 GPa [*Wu et al*., 2016]. Recently, a Mőssbauer study of iron-bearing NAL has shown that ferric and ferrous irons are distributed between two edge-sharing crystallographic sites, *B* and *C*, at ambient conditions [*Wu et al*., 2016]. The trigonal prismatic site *B* hosts both Fe^{2+} and Fe^{3+}, while the octahedral site *C* accommodates Fe^{3+} only. A spin transition in Fe^{3+} at the *C* site occurs at ~40 GPa and 300 K, while the *B* site remains in HS up to at least 80 GPa [*Wu et al*., 2016]). This spin transition of the *C*-site Fe^{3+} and the accompanying volume and elastic anomalies have also been confirmed by a recent first-principles study [*Hsu*, 2017]. Remarkably, the spin transition of the octahedrally coordinated Fe^{3+} in NAL is analogous to that in Bdgm [*Catalli et al*., 2010, 2011; *Hsu et al*., 2012, 2011b; *Yu et al*., 2012]. Hence, changes in the optical absorption of NAL and Bdgm across their respective spin transition must be similar, in accordance with the Tanabe-Sugano diagram for d^5 elements. Other than the aforementioned crystal-chemical similarities with Bdgm, NAL is an abundant mineral in subducting slabs with an estimated content of up to 20% at P = 15–50 GPa [*Ricolleau et al*., 2010] and is a characteristic mineral inclusion in lower mantle diamonds [*Walter et al*., 2011]. Because the spin transition likely affects the partitioning of iron in the NAL-bearing lower mantle, the iron content of NAL inclusions in natural diamonds may be used to infer the *P-T* parameters of the entrapment, similarly to the majorite-garnet composition that has been used to constrain the origin depth of sublithospheric diamonds. The first step toward such a thermobarometer is to characterize the crystal field of NAL across the spin transition.

Here we report room temperature visible and near-infrared (IR) absorption of iron-bearing NAL phase at 0–57 GPa. We confirm the spin transition in Fe^{3+} at the *C* site at 30–47 GPa [*Wu et al*., 2016] and, for the first time, characterize the crystal field of LS ferric iron, establishing the base for optical studies of the spin transition in iron-bearing mixed-valence minerals at lower-mantle pressures. The measured crystal field splitting energy is in excellent agreement with our first-principles calculations based on density functional theory (DFT).

2. Methods

2.1. Experimental Methods

Single crystals of $Na_{0.71}Mg_{2.05}Al_{4.62}Si_{1.16}Fe^{2+}_{0.09}Fe^{3+}_{0.17}O_{12}$ NAL phase (from the same sample capsule of NAL used in a previous study [*Wu et al*., 2016]) were loaded in symmetrical DACs with 300 μm diamond culets. Re gaskets were indented (~45 μm thick) and laser-drilled in the center of the indentation to create a sample chamber (~90–120 μm in diameter). NAL crystals (40–70 μm wide and 10–20 μm thick) were positioned at

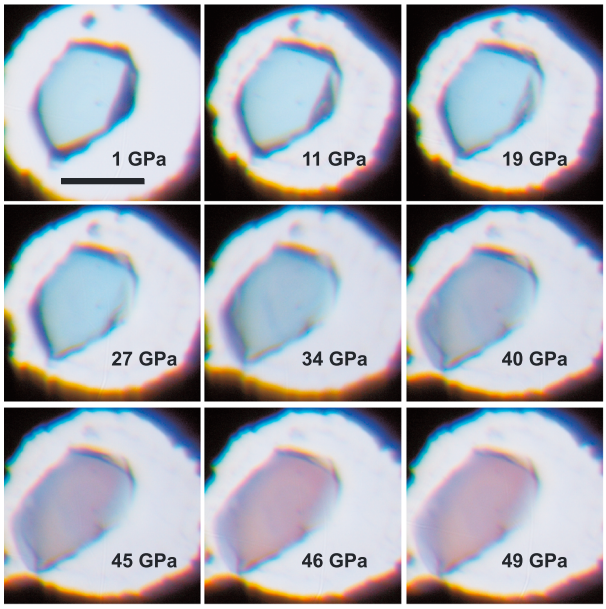

Figure 1. High-pressure optical images of $Na_{0.71}Mg_{2.05}Al_{4.62}Si_{1.16}Fe^{2+}_{0.09}Fe^{3+}_{0.17}O_{12}$ NAL single crystal compressed to ~50 GPa at room temperature taken at identical illumination and image processing conditions. A change in color is observed at ~40 GPa indicating a pressure-induced spin transition. The black bar corresponds to 50 μm.

the center of the cavity with several ruby chips put 10–30 μm aside from the sample for pressure determination. Argon pressure medium was gas-loaded at 0.2 GPa.

Absorption spectra were collected using a custom microscope with all-reflective relay optics in the visible (10,000–25,000 cm^{-1}) and near-mid IR (3000–11,000 cm^{-1}) range. For the visible range we used a fiber-coupled halogen-deuterium light source focused to a ~50 μm spot on the sample. The central portion of the transmitted light (~20 μm) was selected by a confocal aperture and passed to the spectrograph (Acton Research Corporation SpectraPro 500-i) equipped with a 300 grooves/mm grating and a CCD detector operated at 235 K. For the IR range we used a Varian Resolution Pro 670-IR Fourier transform spectrometer with quartz and KBr beamsplitters. The optical setup was described in detail by *Goncharov et al.* [2009]. After the collections in visible and IR ranges, the spectra were stitched together to evaluate the sample optical absorbance: $A(\nu) = -\log_{10}((I_{sample} - I_{bckg})/(I_{reference} - I_{bckg}))$, where I_{sample} is the intensity of light transmitted through the sample, $I_{reference}$ is the intensity of light passed through the pressure medium, and I_{bckg} is the background reading. All spectra were collected at room temperature. Absorption bands were fitted with a Gaussian function after a linear baseline subtraction.

2.2. Theoretical Methods

First-principles calculations based on DFT were performed with the Quantum ESPRESSO codes [*Giannozzi et al.*, 2009]. We used 63-atom supercells (4 × 4 × 4 k-point mesh) of $NaMg_2(Al_5Si)O_{12}$ and $NaMg_2(Al_{4.67}SiFe_{0.33})O_{12}$ to simulate iron-free and iron-bearing (Fe^{3+} in the *C* site) samples, respectively. The atomic configurations of these supercells are detailed in *Hsu* [2017]. The PBE-type generalized gradient approximation (PBE-GGA) [*Perdew et al.*, 1996] and ultrasoft pseudopotentials (USPPs) generated with the Vanderbilt method [*Vanderbilt*, 1990] were adopted in our calculations. The USPPs of Mg, Al, Si, O, and Fe are detailed in *Hsu et al.* [2010]; the USPP of Na is reported in *Garrity et al.* [2014].

3. Experimental Results

Tanabe-Sugano diagrams predict a $^5T_{2g} \rightarrow {}^5E_g$ spin-allowed crystal field absorption band for HS Fe^{2+} and zero spin-allowed transitions for HS Fe^{3+} in NAL phase. Spin-forbidden bands may also be present in the spectra as these may be intensified by magnetic interactions of Fe^{2+} and Fe^{3+} in adjacent edge-sharing *B* and *C* sites [*Burns*, 1993]. Additionally, a Fe^{2+}-Fe^{3+} intervalence charge transfer (CT) may be expected due to the edge-sharing character of the *B* and *C* sites which enhances exchange interactions between the sites [*Burns*, 1993]. LS Fe^{3+} ($^2T_{2g}$ ground state) has four spin-allowed crystal field transitions; thus, the spin crossover in Fe-bearing NAL phase should be optically apparent, consistent with our visual observations of NAL single crystal compressed to ~50 GPa (Figure 1).

At near-ambient conditions, the blue color of iron-bearing NAL phase is due to a single, broad absorption feature at ~14,500 cm^{-1} (Figure 2a). Typical energies of the HS Fe^{2+} crystal field band ($^5T_{2g} \rightarrow {}^5E_g$) in a sixfold coordination (trigonal prismatic site *B*) are 10,000–12,000 cm^{-1}, while Fe^{2+}-Fe^{3+} CT occurs at

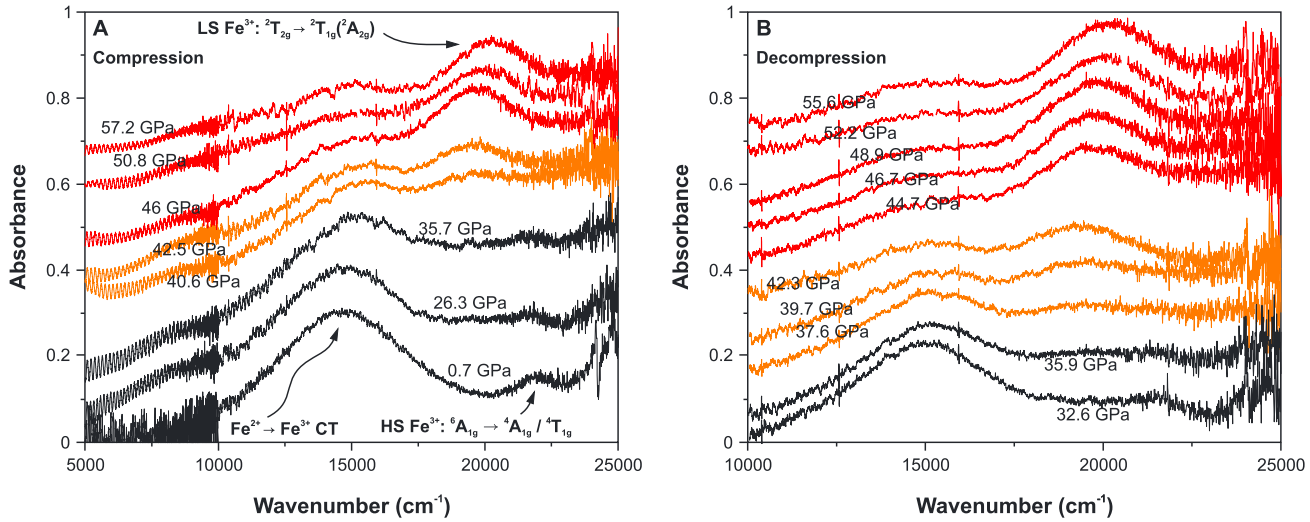

Figure 2. Absorption spectra of $Na_{0.71}Mg_{2.05}Al_{4.62}Si_{1.16}Fe^{2+}_{0.09}Fe^{3+}_{0.17}O_{12}$ NAL upon (a) compression and (b) decompression. Spectra are offset vertically by ~0.1–0.2 for clarity. Significant changes are observed at P ~40 GPa: (i) a new band appears at ~19,200 cm^{-1} and blue-shifts with increasing pressure; (ii) the Fe^{2+}-Fe^{3+} charge transfer (CT) band softens and decreases in intensity. All transformations are reversible on decompression (b), as is expected for a pressure-induced spin transition.

12,000–16,000 cm^{-1} [*Burns*, 1993; *Mattson and Rossman*, 1987]. For this reason we assume that the maximum of absorption intensity at 14,500 cm^{-1} arises from the CT band, obscuring the $^5T_{2g} \rightarrow {}^5E_g$ band which we presume also contributes to the spectrum at 10,000–15,000 cm^{-1}. The broadness of the main absorption feature also relates the band at ~14,500 cm^{-1} to the Fe^{2+}-Fe^{3+} CT as large widths (3000–6500 cm^{-1}) have been diagnostic of the CT bands [*Mattson and Rossman*, 1987].

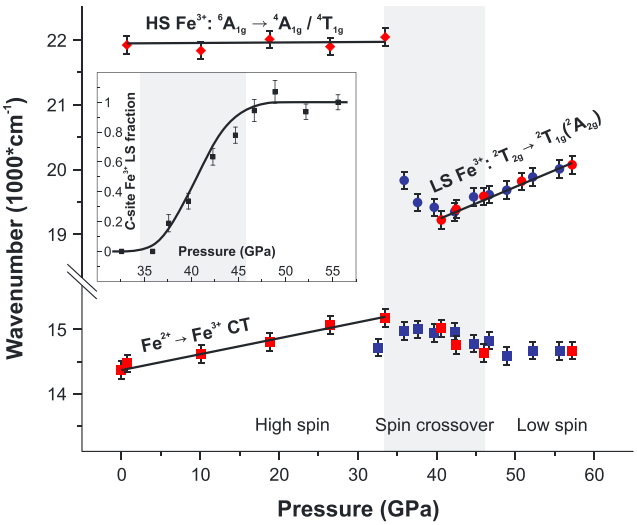

Figure 3. Spectral positions of the absorption bands in NAL phase ($Na_{0.71}Mg_{2.05}Al_{4.62}Si_{1.16}Fe^{2+}_{0.09}Fe^{3+}_{0.17}O_{12}$) at high pressure. Red and blue symbols show compression and decompression data, respectively. Solid lines are linear fits to the positions of the bands. The error bars are 200 cm^{-1} and are due to uncertainties in spectra deconvolution. Inset: Fe^{3+} low spin fraction at site C based on decompression data in Figure 2b and Supplementary Table S1. Error bars are 2*sigma uncertainties to the area of LS Fe^{3+} peak. The grey region corresponds to the spin transition pressure range of a similar NAL sample studied by synchrotron nuclear forward scattering and X-ray diffraction [*Wu et al.*, 2016].

The CT band blue-shifts in the 0–40 GPa pressure range with $d\nu/dP$ = 23 cm^{-1}/GPa (Figure 3). Upon compression to 40–46 GPa, the CT band softens by ~400 cm^{-1} and maintains an approximately constant frequency with further pressure increase. At $P < 40$ GPa, the gradual decrease in intensity is associated with the sample thinning due to compression, while at P ~40 GPa, the CT band intensity reduces abruptly (Figure 2a). Likewise, an increase in the CT band intensity is observed on decompression upon the LS-HS transition while the change in sample thickness is small (Figure 2b). We propose that the magnetic coupling in the Fe^{2+}-Fe^{3+} pair is suppressed across the HS to LS transition as the number of unpaired electrons in Fe^{3+}, which are necessary for the magnetic coupling of the edge-sharing B and C sites [*Cox*, 1980], is reduced from five (HS) to one (LS). Similar intensity

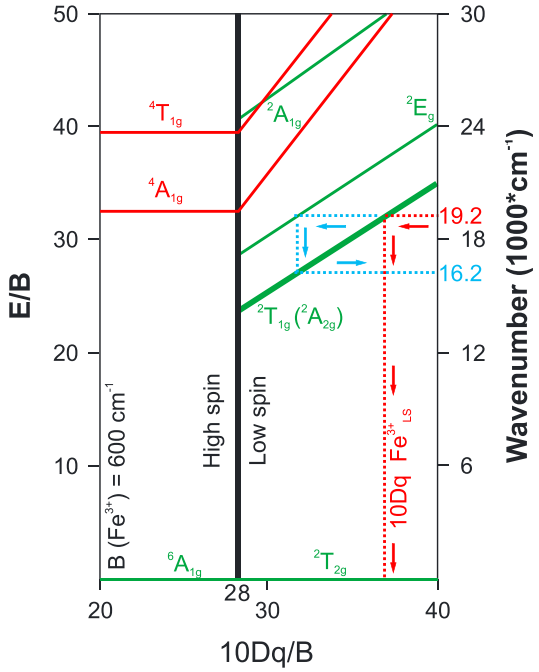

Figure 4. Tanabe-Sugano diagram for *d5* elements in an octahedral crystal field. Green solid lines and labels show spin-allowed transitions and corresponding electronic states. Red solid lines are $^4A_{1g}$ and $^4T_{1g}$ spin-forbidden excited states. Blue dotted line shows that if the band at 19,220 cm^{-1} is due to the ^2E_g spin-allowed excited state, then the $^2T_{2g} \rightarrow {}^2T_{1g}$ ($^2A_{2g}$) band would be expected at ~16,200 cm^{-1}, which is not supported by the absorption data (Figure 3). Therefore, we assign the 19,220 cm^{-1} band to $^2T_{2g} \rightarrow {}^2T_{1g}$ ($^2A_{2g}$). It follows (dotted red line) that the crystal field splitting energy of low spin ferric iron (10DqFe^{3+}_{LS}) is ≈ 22,200 cm^{-1} at 40 GPa. The Racah parameter B = 600 cm^{-1} is assumed consistent with reported values on HS Fe^{3+} [*Burns*, 1993; *Sherman and Waite*, 1985].

variations of the CT band may take place in Bdgm across its spin transition as well as in other iron-bearing mixed-valence compounds, such as post-perovskite (Ppv), increasing the minerals' transparency and, hence, their radiative thermal conductivity. The variations in CT band intensity and spectral position are consistent with the change in color that is seen at ~40 GPa (Figure 1) and, together, represent spectroscopic evidence for the pressure-induced HS-LS transition in NAL.

Another interesting absorption feature of HS NAL is a weak band at 22,000 cm^{-1} that shows no apparent pressure-induced shift (Figures 2 and 3). We propose that this band is due to the $^6A_{1g} \rightarrow {}^4A_{1g}$ or $^6A_{1g} \rightarrow {}^4T_{1g}$ spin-forbidden transitions in HS Fe^{3+} as these do not depend on the crystal field intensity (Figure 4). The definitive choice between these two assignments cannot be made at this time as the Racah parameters derived (B = 675 or 555 cm^{-1} for the $^4A_{1g}$ and $^4T_{1g}$ excited states, respectively) are both consistent with the reported values of B = 540–650 cm^{-1} for HS Fe^{3+} [*Burns*, 1993; *Sherman and Waite*, 1985]. We note, however, that an absorption band at ~22,000 cm^{-1} has been diagnostic of HS Fe^{3+} ions in minerals and is usually assigned to the $^6A_{1g} \rightarrow {}^4A_{1g}$ transition such as in Fe^{3+}-doped Al_2O_3 [*Burns*, 1993].

Simultaneously with the anomalous behavior of the CT band, a new absorption peak centered at ~19,200 cm^{-1} appears in the spectrum (Figure 2a). The new band blue-shifts with increasing pressure (dν/dP = 46 cm^{-1}/GPa), which is characteristic of spin-allowed crystal field bands [*Burns*, 1993], but the pressure shift is much smaller as compared to that for LS Fe^{2+} (88 cm^{-1}/GPa) in a similar crystal field [*Lobanov et al.*, 2015]. The new band intensifies continuously at 37–46 GPa (Figure 3, inset), indicating a growing population of the LS states, in excellent agreement with the C-site Fe^{3+} LS fraction as determined in *Wu et al.* [2016]. At $P > 46$ GPa, this band maintains an approximately constant intensity. At 50.8 GPa, the extinction coefficient of the new band is $\varepsilon \sim 30$ L mole^{-1} cm^{-1}, estimated as $\varepsilon = A*V_{f.u.}*N_A/(d*X)$, where A = 0.08 is the sample absorbance at the center of the new band (Figure 2a), $V_{f.u.}$ is the NAL volume per formula unit in liters (7.84×10^{-26} at 51 GPa [*Wu et al.*, 2016]), N_A is the Avogadro's number, d = 0.0015 cm is the sample thickness, and X = 0.085 is the Fe^{3+} molar fraction at the octahedral site [*Wu et al.*, 2016]. Our estimate is in the range of extinction coefficients of spin-allowed crystal field bands [*Figgis*, 1966] suggesting that the new band is of crystal field origin (*d-d* band). Accordingly, we assign the band at ~19,200 cm^{-1} to the lowest energy spin-allowed excited state $^2T_{1g}$ ($^2A_{2g}$) in LS Fe^{3+} (Figure 4). We have a rough check on this assignment by accepting the Racah parameter B = 600 cm^{-1}, based on the reported values of B = 540–650 cm^{-1} for ferric iron in an octahedral coordination [*Burns*, 1993; *Sherman and Waite*, 1985], allowing to estimate the crystal field splitting energy of LS Fe^{3+} (10DqFe^{3+}_{LS} ≈ 22,200 cm^{-1}) as outlined in Figure 4 (dotted red line). At ambient conditions, crystal field splitting energies of HS Fe^{3+} in iron oxides and hydroxides are in the range of 14,000–16,000 cm^{-1} [*Sherman and Waite*, 1985]). Accepting a pressure shift of ~100 cm^{-1}/GPa [*Mao and Bell*, 1974],

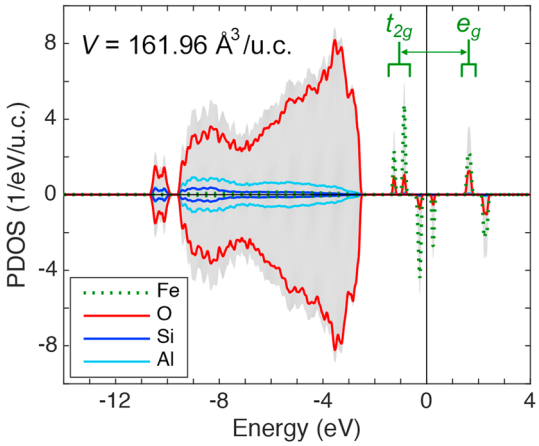

Figure 5. Projected (lines) and total (shade) density of states of $NaMg_2(Al_{4.67},Fe_{0.33},Si)O_{12}$ with LS Fe^{3+} substituting Al in the *C* site. At the unit cell V = 161.96 Å^3 ($P \approx 40$ GPa), the crystal field splitting (indicated by the double-headed arrow) is ~2.7 eV (~21,800 cm^{-1}), in excellent agreement with 22,000 cm^{-1} as derived from the Tanabe-Sugano diagram in Figure 4.

we obtain $10DqFe^{3+}_{HS} \approx$ 18,000–20,000 cm^{-1} at 40 GPa. Across the spin transition, 10Dq increases abruptly as a result of a discontinuous Fe-O bond shortening. For example, an increase in 10Dq of ~4000 cm^{-1} is observed in the octahedrally coordinated Fe^{2+} in siderite ($FeCO_3$) across the spin transition [*Lobanov et al.*, 2015]. Taking this into consideration, we obtain $10DqFe^{3+}_{LS} \approx$ 22,000–24,000 cm^{-1}, close to what we have evaluated from the Tanabe-Sugano diagram (Figure 4) and, therefore, consistent with the assignment of the new band to the ground-to-lowest energy excited state transition in LS Fe^{3+} ($^2T_{2g} \rightarrow {}^2T_{1g}$ ($^2A_{2g}$)).

A decompression run shows that all the observed variations in optical absorbance are reversible (Figure 2b), also consistent with the spin transition scenario. However, a small hysteresis was observed for the low-to-high spin transition such that the $^2T_{2g} \rightarrow {}^2T_{1g}$ ($^2A_{2g}$) band was present in the spectra down to ~37 GPa (Figures 2b and 3). Interestingly, the new band reverses the sign of its frequency-pressure shift upon decompression below 44 GPa (Figure 3), indicating an increase in the crystal field splitting energy at the LS Fe^{3+} site upon the LS to HS transformation. This very unusual behavior suggests that the growing number of HS $Fe^{3+}O_6$ units induces local strain in the lattice, imposing additional stress to the yet untransformed LS Fe^{3+} sites.

4. Theoretical Results

To verify that the ~19,200 cm^{-1} band is a result of the $^2T_{2g} \rightarrow {}^2T_{1g}$ ($^2A_{2g}$) transition, we computed the crystal field splitting (10Dq) of the LS *C*-site Fe^{3+} in NAL. Using PBE-GGA, we optimized a 63-atom supercell of NAL with one single LS Fe^{3+} substituting Al in the *C* site, namely $NaMg_2(Al_{4.67}SiFe_{0.33})O_{12}$, at the cell volume V = 161.96 Å^3/f.u., same as observed at $P \approx 40$ GPa that marks the beginning of the HS-LS transition [*Wu et al.*, 2016]. The resultant electronic structure (PBE-GGA) is shown in Figure 5, where the projected density of states (PDOS) onto each atomic species and the total DOS are plotted, with an energy resolution of 0.02 eV. Indicated by the nonzero band gap, PBE-GGA correctly predicts an insulating LS state without the inclusion of the Hubbard *U* correction. The orbital occupancy and electron charge density of the LS *C*-Fe^{3+} determined by PBE-GGA would thus be accurate, too, as discussed in *Hsu et al.* [2011a]. It should be emphasized, however, that the Hubbard *U* correction is still necessary to treat iron in other spin states (and thus the spin transition) in the NAL phase, as detailed in *Hsu* [2017]. As shown in Figure 5, the Fe *3d* orbitals form several narrow bands around the Fermi level E_F (set to zero), giving rise to the Fe PDOS peaks indicated by the green (dotted) line. In the spin-up channel, the two Fe PDOS peaks below E_F and the one Fe PDOS peak above E_F correspond to the filled t_{2g} and empty e_g bands, respectively. The formation of two t_{2g} bands indicates that the three t_{2g} orbitals are nondegenerate due to the distorted $Fe^{3+}O_6$ octahedra, which leads to the broadness of the $^2T_{2g} \rightarrow {}^2T_{1g}$ ($^2A_{2g}$) absorption band. The two e_g orbitals are still degenerate; only one e_g band is formed. The crystal field splitting, derived from the energy difference between the centers of the t_{2g} and e_g bands, is ~2.7 eV (~21,800 cm^{-1}), in excellent agreement with 22,000 cm^{-1} derived from the Tanabe-Sugano diagram (Figure 4) within the experimental uncertainty (200 cm^{-1}). Furthermore, DFT calculation shows that 10Dq increases with pressure (not presented here), consistent with the blue-shift of the $^2T_{2g} \rightarrow {}^2T_{1g}$ ($^2A_{2g}$) band observed at $P > 40$ GPa shown in Figure 3.

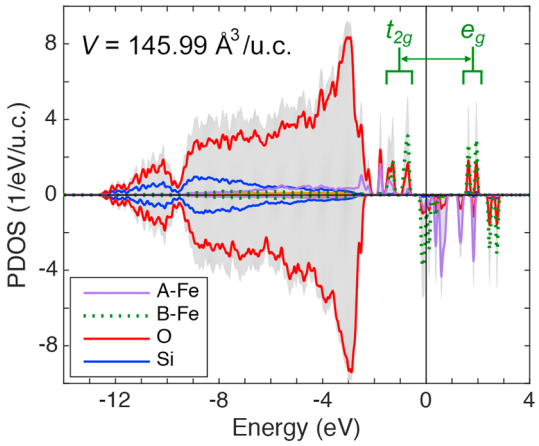

Figure 6. Projected (lines) and total (shade) density of states of $(Mg_{0.875}Fe_{0.125})(Si_{0.875}\ Fe_{0.125})O_3$ Bdgm. At the unit cell V = 145.99 Å^3 ($P \approx$ 40 GPa), the crystal field splitting (indicated by the double-headed arrow) is ~2.8 eV (~22,600 cm^{-1}).

Similar to the NAL phase, we determined the crystal field splitting of LS Fe^{3+} at the B site in $(Mg_{0.875}Fe_{0.125})(Si_{0.875}Fe_{0.125})O_3$ Bdgm with HS Fe^{3+} at the dodecahedral A site and LS Fe^{3+} at the B site. At V = 145.99 Å^3/cell, which marks the beginning of HS-LS transition observed in experiment at ~45 GPa [*Catalli et al.*, 2010], the separation between the t_{2g} and e_g bands is ~2.8 eV (22,600 cm^{-1}) (Figure 6), close to the crystal field splitting energy in LS NAL at 40 GPa (Figures 4 and 5).

5. Discussion

Spin transitions occur when the crystal field splitting energy of a cation (10Dq) exceeds its site-specific *d-d* spin-pairing energy (E_p). This study constrains the crystal field splitting energy of LS Fe^{3+} at the octahedral site of NAL to $10Dq_{LS}^{3+}$ = 22,200 cm^{-1} at 40 GPa. This is in excellent agreement with the optical measurements of E_p = 20,600–22,900 cm^{-1} of Fe^{3+} in the strong octahedral field of $Fe(S_2CNR_2)_3$ at 1 atm [*Ewald et al.*, 1969]. Indeed, due to the nephelauxetic effect the spin-pairing energy of a cation in a crystal field is 70–85% of the field-free cation value (29,875 cm^{-1} for field-free Fe^{3+}) [*Burns*, 1993]. Figure 7 compares the optically derived 10Dq values of iron-bearing NAL as well as of other phases to the corresponding E_p estimates for Fe^{2+} and Fe^{3+}. Crystal field splitting energies of HS and LS iron appear consistent with the corresponding spin-pairing energy. For example, direct optical measurements of the crystal field splitting energy of HS and LS siderite show a straightforward behavior in that $10Dq_{HS}^{2+} < E_p$ and $10Dq_{LS}^{2+} > E_p$. Likewise, the available spectroscopic data on the electronic structure of octahedrally coordinated Fe^{3+} suggests that its spin-pairing energy is $E_p \approx$ 20,000–23,000 cm^{-1} (Figure 7). Our DFT computations of the crystal field splitting energy in Bdgm (Figure 6) yielded $10Dq_{Bdgm}$ = 22,600 cm^{-1} for LS Fe^{3+} at the octahedral site at

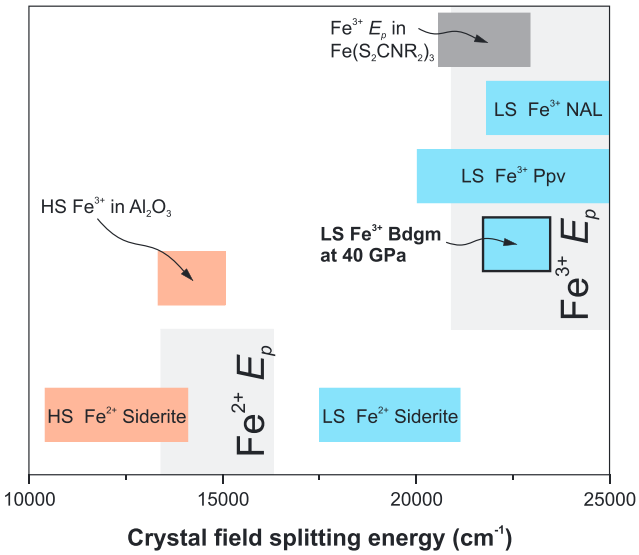

Figure 7. Crystal field splitting energies of iron in an octahedral crystal field of NAL (this study), post-perovskite (Ppv) [*Lobanov et al.*, 2016b], and siderite [*Lobanov et al.*, 2015] as deduced from optical absorption measurements in DACs at 300 K. Red and blue horizontal bars show high and low spin values, respectively. The crystal field splitting energy of LS Fe^{3+} in Bdgm is computed in this work (Figure 6). Light grey vertical bars are approximate spin-pairing energies (E_p) of ferric and ferrous iron in a crystal field (estimated as 75–80% of the spin-pairing energy for the field-free cations [*Burns*, 1993]). Dark grey bar is E_p in $Fe(S_2CNR_2)_3$, which contains LS Fe^{3+} in an octahedral field, as deduced from optical measurements across the temperature-induced spin transition [*Ewald et al.*, 1969]. The crystal field splitting energy of Fe^{3+}-bearing corundum is at 1 atm [*Burns*, 1993].

$P \approx 40$ GPa. This value suggests that the theory-based view of the *B*-site Fe^{3+} spin transition in Bdgm at $P > 40$ GPa [*Hsu et al*., 2010, 2011b; *Yu et al*., 2012] is consistent with the direct spectroscopic constraints on the spin-pairing energy in $Fe^{3+}O_6$ compounds (Figure 7), such as determined in this work.

This empirical inference can be tested by direct optical observations of a spin transition in Bdgm, for which this work provides an important spectroscopic reference: the $^2T_{2g} \rightarrow {}^2T_{1g}$ ($^2A_{2g}$) band at ~17,000–22,000 cm^{-1} is characteristic of octahedrally coordinated LS Fe^{3+}. This is justified by the d^5 Tanabe-Sugano diagram as well as the similarity in 10Dq of LS NAL and Bdgm. In further support, an absorption band centered at ~17,500 cm^{-1} is present in the absorption spectra of LS Fe^{3+}-bearing $Mg_{0.6}Fe_{0.4}SiO_3$ post-perovskite at 130 GPa and 300 K [*Lobanov et al*., 2016b] which resembles NAL and Bdgm in the distribution of iron in the crystal structure [*Hsu et al*., 2012; *Wu et al*., 2016; *Yu et al*., 2012]. It is clear, however, that the intensity of the $^2T_{2g} \rightarrow {}^2T_{1g}$ ($^2A_{2g}$) band is proportional to iron concentration at the octahedral site; thus, a substantial amount of LS Fe^{3+} (~10 mol. %) is needed to detect the band. The overall solubility of Fe^{3+} in Bdgm is enhanced by Al^{3+} [e.g., *Lauterbach et al*., 2000; *McCammon*, 1997; *Sinmyo et al*., 2011], but the predominant incorporation of Al^{3+} in the octahedral *B* site limits the concentration of Fe^{3+} at this position. As a result, we expect Fe^{3+} to mostly occupy the *A* site in Bdgm with a mole fraction of $Al^{3+} > Fe^{3+}$ [*Kupenko et al*., 2015; *Potapkin et al*., 2013]. A recent combined XES and Mössbauer study of the iron spin state in Al-bearing Bdgm with almost all Fe^{2+} and Fe^{3+} in the *A* site has revealed that these iron ions remain in the HS state at lower-mantle pressures [*Lin et al*., 2016]. Therefore, all iron in Bdgm with $Al^{3+} > Fe^{3+}$ is likely in the HS configuration at the conditions of Earth's lower mantle. It follows that the theoretically proposed spin transition scenario for Fe^{3+} at the *B* site [*Hsu and Wentzcovitch*, 2014; *Hsu et al*., 2012, 2010, 2011b; *Mohn and Trønnes*, 2016; *Yu et al*., 2012; *Zhang and Oganov*, 2006] may be achieved in samples with $Al^{3+} < Fe^{3+}$, but available high-pressure optical absorption data on Bdgm with variable $Fe^{3+}/\Sigma Fe$ and Al^{3+} content are limited and inconclusive in addressing the spin state of iron [*Goncharov et al*., 2008]. For instance, the $^2T_{2g} \rightarrow {}^2T_{1g}$ ($^2A_{2g}$) band was not detected in the absorption spectra of $Mg_{0.9}Fe_{0.1}SiO_3$ (11 ± 3% Fe^{3+}) [*Goncharov et al*., 2008] up to the highest pressure of ~130 GPa. The presence/absence of Fe^{3+} at the *B* site, however, has not been reported for this sample, and it is unclear whether the absence of the $^2T_{2g} \rightarrow {}^2T_{1g}$ ($^2A_{2g}$) band is due to the exclusive HS iron configuration in the studied pressure range or due to the lack of Fe^{3+} at the octahedral site. In the future, systematic optical studies of Bdgm with variable compositions (Fe^{2+}, Fe^{3+}, Al^{3+}) at high pressure will help resolve this controversy in the Bdgm spin state.

Acknowledgments

This work was supported by the NSF Major Research Instrumentation program, NSF EAR-1015239, NSF EAR-1520648 and NSF EAR/IF-1128867, the Army Research Office (56122-CH-H), and the Carnegie Institution of Washington and Deep Carbon Observatory. S.S.L. was partly supported by the state assignment project 0330-2016-0006. H.H. is supported by the Ministry of Science and Technology of Taiwan under grant MOST 104-2112-M-008-005-MY3. J.F.L. acknowledges support from the NSF Geophysics Program and CSEDI (EAR1446946, EAR1502594). A.F.G. was partly supported by the Chinese Academy of Sciences visiting professorship for senior international scientists (grant 2011T2J20), Recruitment Program of Foreign Expert, the National Natural Science Foundation of China (grant 21473211), and the Chinese Academy of Sciences (grant YZ201524). T.Y. acknowledges support from the JSPS MEXT/KAKENHI Grant Number JP15H05827. Portions of this work were performed at GeoSoilEnviroCARS (Sector 13), Advanced Photon Source (APS), and Argonne National Laboratory. GeoSoilEnviroCARS is supported by the National Science Foundation—Earth Sciences (EAR-1128799) and Department of Energy—GeoSciences (DE-FG02-94ER14466). This research used resources of the Advanced Photon Source, a U.S. Department of Energy (DOE) Office of Science User Facility operated for the DOE Office of Science by Argonne National Laboratory under contract DE-AC02-06CH11357. We thank S. Fu and J. Yang for helping with polishing the crystals as well as Zachary Geballe and Nicholas Holtgrewe for their comments on the earlier versions of this manuscript. Data associated with this paper are available through e-mail requests send to the corresponding author.

References

Badro, J. (2014), Spin transitions in mantle minerals, *Annu. Rev. Earth Planet. Sci.*, *42*, 231–248.

Badro, J., G. Fiquet, F. Guyot, J. P. Rueff, V. V. Struzhkin, G. Vanko, and G. Monaco (2003), Iron partitioning in Earth's mantle: Toward a deep lower mantle discontinuity, *Science*, *300*(5620), 789–791.

Badro, J., J. P. Rueff, G. Vanko, G. Monaco, G. Fiquet, and F. Guyot (2004), Electronic transitions in perovskite: Possible nonconvecting layers in the lower mantle, *Science*, *305*(5682), 383–386.

Burns, R. G. (1993), *Mineralogical Applications of Crystal Field Theory*, 2nd ed., 551 pp., Cambridge Univ. Press, U. K.

Catalli, K., S. H. Shim, V. B. Prakapenka, J. Y. Zhao, W. Sturhahn, P. Chow, Y. M. Xiao, H. Z. Liu, H. Cynn, and W. J. Evans (2010), Spin state of ferric iron in $MgSiO_3$ perovskite and its effect on elastic properties, *Earth Planet. Sci. Lett.*, *289*(1–2), 68–75.

Catalli, K., S. H. Shim, P. Dera, V. B. Prakapenka, J. Y. Zhao, W. Sturhahn, P. Chow, Y. M. Xiao, H. Cynn, and W. J. Evans (2011), Effects of the Fe^{3+} spin transition on the properties of aluminous perovskite—New insights for lower-mantle seismic heterogeneities, *Earth Planet. Sci. Lett.*, *310*(3–4), 293–302.

Cox, P. A. (1980), Electron transfer between exchange-coupled ions in a mixed-valency compound, *Chem. Phys. Lett.*, *69*(2), 340–343.

Dorfman, S. M., J. Badro, J. P. Rueff, P. Chow, Y. M. Xiao, and P. Gillet (2015), Composition dependence of spin transition in $(Mg,Fe)SiO_3$ bridgmanite, *Am. Mineral.*, *100*(10), 2246–2253.

Dyar, M. D., D. G. Agresti, M. W. Schaefer, C. A. Grant, and E. C. Sklute (2006), Mössbauer spectroscopy of Earth and planetary materials, *Annu. Rev. Earth Planet. Sci.*, *34*, 83–125.

Ewald, A. H., R. L. Martin, E. Sinn, and A. H. White (1969), Electronic equilibrium between the $^6A_1$ and $^2T_2$ states in iron(III) dithio chelates, *Inorg. Chem.*, *8*(9), 1837–1846.

Figgis, B. N. (1966), *Introduction to Ligand Fields*, p. 351, Interscience, New York.

Garrity, K. F., J. W. Bennett, K. M. Rabe, and D. Vanderbilt (2014), Pseudopotentials for high-throughput DFT calculations, *Comput. Mater. Sci.*, *81*, 446–452.

Giannozzi, P., et al. (2009), QUANTUM ESPRESSO: A modular and open-source software project for quantum simulations of materials, *J. Phys. Condens. Matter*, *21*(39), 395502.

Goncharov, A. F., V. V. Struzhkin, and S. D. Jacobsen (2006), Reduced radiative conductivity of low-spin (Mg,Fe)O in the lower mantle, *Science*, *312*(5777), 1205–1208.

Goncharov, A. F., B. D. Haugen, V. V. Struzhkin, P. Beck, and S. D. Jacobsen (2008), Radiative conductivity in the Earth's lower mantle, *Nature*, *456*(7219), 231–234.

Goncharov, A. F., P. Beck, V. V. Struzhkin, B. D. Haugen, and S. D. Jacobsen (2009), Thermal conductivity of lower-mantle minerals, *Phys. Earth Planet. In.*, *174*(1–4), 24–32.
Hsu, H. (2017), First-principles study of iron spin crossover in the new hexagonal aluminous phase, *Phys. Rev. B*, *95*(2), 020406.
Hsu, H., and R. M. Wentzcovitch (2014), First-principles study of intermediate-spin ferrous iron in the Earth's lower mantle, *Phys. Rev. B*, *90*(19), 195205.
Hsu, H., K. Umemoto, P. Blaha, and R. M. Wentzcovitch (2010), Spin states and hyperfine interactions of iron in (Mg,Fe)SiO_3 perovskite under pressure, *Earth Planet. Sci. Lett.*, *294*(1–2), 19–26.
Hsu, H., K. Umemoto, M. Cococcioni, and R. M. Wentzcovitch (2011a), The Hubbard U correction for iron-bearing minerals: A discussion based on (Mg,Fe)SiO_3 perovskite, *Phys. Earth Planet. In.*, *185*(1–2), 13–19.
Hsu, H., P. Blaha, M. Cococcioni, and R. M. Wentzcovitch (2011b), Spin-state crossover and hyperfine interactions of ferric iron in $MgSiO_3$ perovskite, *Phys. Rev. Lett.*, *106*(11), 118,501.
Hsu, H., Y. G. G. Yu, and R. M. Wentzcovitch (2012), Spin crossover of iron in aluminous $MgSiO_3$ perovskite and post-perovskite, *Earth Planet. Sci. Lett.*, *359*, 34–39.
Huang, C., W. Leng, and Z. Q. Wu (2015), Iron-spin transition controls structure and stability of LLSVPs in the lower mantle, *Earth Planet. Sci. Lett.*, *423*, 173–181.
Hummer, D. R., and Y. W. Fei (2012), Synthesis and crystal chemistry of Fe^{3+}-bearing (Mg,Fe^{3+})(Si,Fe^{3+})O_3 perovskite, *Am. Mineral.*, *97*(11–12), 1915–1921.
Keppler, H., I. Kantor, and L. S. Dubrovinsky (2007), Optical absorption spectra of ferropericlase to 84 GPa, *Am. Mineral.*, *92*(2–3), 433–436.
Keppler, H., L. S. Dubrovinsky, O. Narygina, and I. Kantor (2008), Optical absorption and radiative thermal conductivity of silicate perovskite to 125 Gigapascals, *Science*, *322*(5907), 1529–1532.
Kupenko, I., C. McCammon, R. Sinmyo, V. Cerantola, V. Potapkin, A. I. Chumakov, A. Kantor, R. Ruffer, and L. Dubrovinsky (2015), Oxidation state of the lower mantle: In situ observations of the iron electronic configuration in bridgmanite at extreme conditions, *Earth Planet. Sci. Lett.*, *423*, 78–86.
Lauterbach, S., C. A. McCammon, P. van Aken, F. Langenhorst, and F. Seifert (2000), Mossbauer and ELNES spectroscopy of (Mg,Fe)(Si,Al)O_3 perovskite: A highly oxidised component of the lower mantle, *Contrib. Mineral. Petrol.*, *138*(1), 17–26.
Li, J., V. V. Struzhkin, H. K. Mao, J. F. Shu, R. J. Hemley, Y. W. Fei, B. Mysen, P. Dera, V. Prakapenka, and G. Y. Shen (2004), Electronic spin state of iron in lower mantle perovskite, *Proc. Natl. Acad. Sci. U. S. A.*, *101*(39), 14027–14030.
Lin, J. F., E. E. Alp, Z. Mao, T. Inoue, C. McCammon, Y. M. Xia, P. Chow, and J. Y. Zhao (2012), Electronic spin states of ferric and ferrous iron in the lower-mantle silicate perovskite, *Am. Mineral.*, *97*(4), 592–597.
Lin, J. F., S. Speziale, Z. Mao, and H. Marquardt (2013), Effects of the electronic spin transitions of iron in lower mantle minerals: Implications for deep mantle geophysics and geochemistry, *Rev. Geophys.*, *51*, 244–275, doi:10.1002/rog.20010.
Lin, J. F., Z. Mao, J. Yang, J. Liu, Y. Xiao, P. Chow, and T. Okuchi (2016), High-spin Fe^{2+} and Fe^{3+} in single-crystal aluminous bridgmanite in the lower mantle, *Geophys. Res. Lett.*, *43*, 6952–6959, doi:10.1002/2016GL069836.
Lobanov, S. S., A. F. Goncharov, and K. D. Litasov (2015), Optical properties of siderite ($FeCO_3$) across the spin transition: Crossover to iron-rich carbonates in the lower mantle, *Am. Mineral.*, *100*(5–6), 1059–1064.
Lobanov, S. S., N. Holtgrewe, and A. F. Goncharov (2016a), Reduced radiative conductivity of low spin FeO_6-octahedra in $FeCO_3$ at high pressure and temperature, *Earth Planet. Sci. Lett.*, *449*, 20–25.
Lobanov, S. S., N. Holtgrewe, J. F. Lin, and A. F. Goncharov (2016b), Radiative conductivity and abundance of post-perovskite in the lowermost mantle, *arXiv*, arXiv:1609.06996.
Mao, H. K., and P. M. Bell (1974), Crystal-field effects of ferric iron in goethite and lepidocrocite: Band assignments and geochemical application at high pressure, *Carnegie Institute of Washington Yearbook*, *1973*, 502–507.
Marquardt, H., S. Speziale, H. J. Reichmann, D. J. Frost, F. R. Schilling, and E. J. Garnero (2009), Elastic shear anisotropy of ferropericlase in Earth's lower mantle, *Science*, *324*(5924), 224–226.
Mattson, S. M., and G. R. Rossman (1987), Identifying characteristics of charge transfer transitions in minerals, *Phys. Chem. Miner.*, *14*(1), 94–99.
McCammon, C. (1997), Perovskite as a possible sink for ferric iron in the lower mantle, *Nature*, *387*(6634), 694–696.
McCammon, C., L. Dubrovinsky, O. Narygina, I. Kantor, X. Wu, K. Glazyrin, I. Sergueev, and A. I. Chumakov (2010), Low-spin Fe^{2+} in silicate perovskite and a possible layer at the base of the lower mantle, *Phys. Earth Planet. In.*, *180*(3–4), 215–221.
Mohn, C. E., and R. G. Trønnes (2016), Iron spin state and site distribution in $FeAlO_3$-bearing bridgmanite, *Earth Planet. Sci. Lett.*, *440*, 178–186.
Perdew, J. P., K. Burke, and M. Ernzerhof (1996), Generalized gradient approximation made simple, *Phys. Rev. Lett.*, *77*(18), 3865–3868.
Potapkin, V., et al. (2013), Effect of iron oxidation state on the electrical conductivity of the Earth's lower mantle, *Nat. Commun.*, *4*, 1427.
Ricolleau, A., J. P. Perrillat, G. Fiquet, I. Daniel, J. Matas, A. Addad, N. Menguy, H. Cardon, M. Mezouar, and N. Guignot (2010), Phase relations and equation of state of a natural MORB: Implications for the density profile of subducted oceanic crust in the Earth's lower mantle, *J. Geophys. Res.*, *115*, B08202, doi:10.1029/2009JB006709.
Sherman, D. M., and T. D. Waite (1985), Electronic spectra of Fe^{3+} oxides and oxide hydroxides in the near IR to near UV, *Am. Mineral.*, *70*(11–12), 1262–1269.
Sinmyo, R., K. Hirose, S. Muto, Y. Ohishi, and A. Yasuhara (2011), The valence state and partitioning of iron in the Earth's lowermost mantle, *J. Geophys. Res.*, *116*, B07205, doi:10.1029/2010JB008179.
Vanderbilt, D. (1990), Soft self-consistent pseudopotentials in a generalized eigenvalue formalism, *Phys. Rev. B*, *41*(11), 7892–7895.
Vilella, K., S. H. Shim, C. G. Farnetani, and J. Badro (2015), Spin state transition and partitioning of iron: Effects on mantle dynamics, *Earth Planet. Sci. Lett.*, *417*, 57–66.
Walter, M. J., S. C. Kohn, D. Araujo, G. P. Bulanova, C. B. Smith, E. Gaillou, J. Wang, A. Steele, and S. B. Shirey (2011), Deep mantle cycling of oceanic crust: Evidence from diamonds and their mineral inclusions, *Science*, *334*(6052), 54–57.
Wu, Y., X. Wu, J. F. Lin, C. A. McCammon, Y. M. Xiao, P. Chow, V. B. Prakapenka, T. Yoshino, S. M. Zhai, and S. Qin (2016), Spin transition of ferric iron in the NAL phase: Implications for the seismic heterogeneities of subducted slabs in the lower mantle, *Earth Planet. Sci. Lett.*, *434*, 91–100.
Yang, J., X. Y. Tong, J. F. Lin, T. Okuchi, and N. Tomioka (2015), Elasticity of ferropericlase across the spin crossover in the Earth's lower mantle, *Sci. Rep-Uk*, *5*, 17,188.
Yu, Y. G. G., H. Hsu, M. Cococcioni, and R. M. Wentzcovitch (2012), Spin states and hyperfine interactions of iron incorporated in $MgSiO_3$ post-perovskite, *Earth Planet. Sci. Lett.*, *331*, 1–7.
Zhang, F. W., and A. R. Oganov (2006), Valence state and spin transitions of iron in Earth's mantle silicates, *Earth Planet. Sci. Lett.*, *249*(3–4), 436–443.